An extended-range improvement solution for a homing flight vehicle

Nguyen Van Khoi, Trinh Anh Minh, Nguyen Quang Vinh*

Institute of Missile, Academy of Military Science and Technology, 17 Hoang Sam, Nghia Do, Hanoi, Vietnam.
*Corresponding author: vinhquang2808@gmail.com
Received 05 Jan. 2026; Revised 25 Feb. 2026; Accepted 02 Mar. 2026; Published 25May 2026.
DOI: https://doi.org/10.54939/1859-1043.j.mst.111.2026.12-21

ABSTRACT

This paper presents an extended-range improvement solution for a controlled gliding flight vehicle (GFV) equipped with a TV-homing seeker by increasing the lifting surface area within allowable limits while preserving static stability. This modification requires a redesign of the flight control system to accommodate the new aerodynamic configuration. Furthermore, during extended-range gliding flight, the vehicle experiences significant variations in velocity and altitude; therefore, the designed controller must ensure robustness over the entire flight envelope and under external disturbances. Six-degree-of-freedom (6DOF) simulation results demonstrate that the proposed improvement Solution and synthesized control system enable the GFV to increase its operational range from 9 km to 16 km while maintaining a terminal impact angle of no less than 45 degrees.

Keywords: Extended-range gliding flight vehicle; Control system synthesis; 6DOF simulation.

1. INTRODUCTION

Recent advances in science and technology have enabled significant performance improvements for various weapon systems. Worldwide, extended-range enhancement solutions for gliding flight vehicles (GFVs) mainly follow two principal approaches.

The first approach employs additional wing kits to convert conventional free-fall munitions into controlled GFVs [1–6]. This solution typically integrates an INS/GPS-based guidance system and a tail control system to execute guidance laws toward a predefined target location.

The second approach focuses on modifying the aerodynamic configuration to increase lift, thereby extending the range of controlled GFVs [7-8]. This approach is usually applied to vehicles equipped with advanced homing seekers, allowing to lock on target acquisition at longer distances.

In this paper, the authors focus on the second approach and propose an extended-range improvement Solution for a controlled GFV [9].

Most published studies related to this approach concentrate on replacing a four-wing configuration with two larger lifting surfaces [10,11]. While this configuration is suitable for subsonic Gliding flight vehicles (GFV), it presents installation challenges due to space limitations on carrier aircraft. Foldable wing solutions have been investigated [6], but they require additional mechanical deployment, increasing system complexity. In practice, current TV-homing GFVs achieve maximum target lock-on ranges of approximately 15–16 km. Consequently, a simpler and more feasible solution is to increase the wing area to achieve the desired range extension. However, this solution entails addressing two key technical challenges.

First, the guidance and control system must be modified to ensure both terminal accuracy and the required impact angle with the target.

Second, to guarantee that the proposed modification does not affect pilot operation on the carrier aircraft, it is necessary to clearly understand the information exchange process between the carrier aircraft and the HFV.

Although numerous studies worldwide address guidance and control design for extended-range gliding vehicles, a comprehensive publication covering guidance law synthesis, control system

design, and validation through 6DOF simulation remains limited. Ahmed [9] developed a 6DOF model and a guidance loop for a TV-homing gliding bomb using a PD controller; however, 6DOF simulation validation was not provided. Similarly, [10] focused on classical PID and modified PI-D controllers without closing the homing guidance loop. Study [2] addressed 6DOF modeling and simulation under wind disturbances but excluded guidance and control loops. In [3], a complete guidance and control solution with 6DOF simulation was presented, yet parameter variations and disturbances were not considered. In [7], a PID-SMC controller combined with proportional navigation (PN) guidance was proposed; however, this approach is unsuitable for extended-range GFVs due to the resulting small terminal impact angle. To improve controller performance under large velocity and altitude variations, Gian [12] proposed an autopilot based on Linear Parameter-Varying (LPV) techniques; nevertheless, robustness against disturbances and uncertainties was discussed without simulation verification on a specific vehicle.

Regarding the second challenge, the complete communication cycle between the carrier aircraft and the HFV in combat applications can be obtained through fire-control system test equipment. For example, the communication characteristics of the KAB-500 integrated with the Su-30 aircraft can be identified using the AKPA-30(27) test system. Test results provide time-sequenced information such as HFV payload status (Нал.груза), power supply modes (27 V, 36/400 Hz, 36/1000 Hz), seeker operating states (ЗГ, СГ), television signal channels (ССИ, КСИ, ВС), target signals (Цель), and release modes (Ав.сброс, Взрыв).

Therefore, based on an extended-range improvement Solution for a controlled gliding flight vehicle, this paper synthesizes a complete guidance and control system and validates its robustness through 6DOF simulation under parameter variations and external disturbances.

2. PROBLEM

2.1. Extended-range improvement scheme

The original GFV (Figure 1), equipped with a TV-homing seeker, is released from an aircraft at a maximum speed of 1100 km/h and a maximum altitude of 5 km, with an effective engagement range of up to 9 km. With advances in TV seeker technology enabling target acquisition at significantly longer distances, the proposed solution involves relocating and increasing the area of the forward lifting wings. This modification preserves the original vehicle structure and aircraft mounting configuration while achieving the extended-range objective.

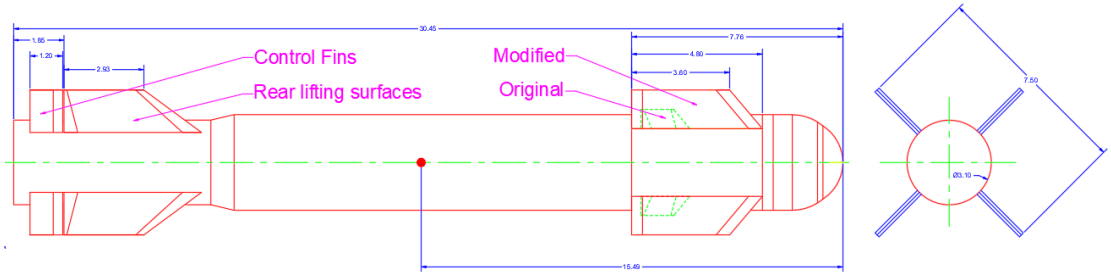

Figure 1. *Extended-range improvement scheme for the controlled GFV.*

With this improvement, the static stability margin Xcp decreases from 2.46 to 1.45, ensuring both stability and enhanced range controllability. In practice, for GFVs requiring high maneuverability, this parameter is usually set between 0.7 and 1.2. For GFVs attacking fixed targets, this value is usually greater than 1.2. However, due to geometric limitations, the value of 1.45 corresponds to the largest allowable size of the modified design. Simulation results comparing the original and modified configurations are shown in Figure 2.

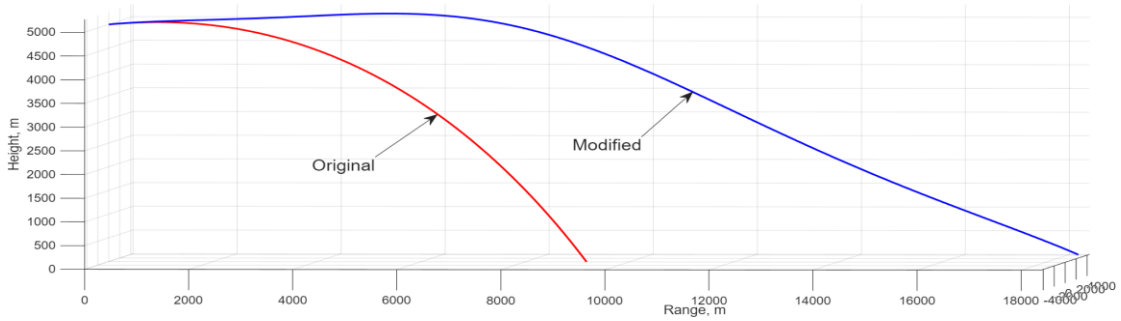

Figure 2. *Simulation results of the original and modified controlled GFV.*

2.2. Six-degree-of-freedom motion model

The proposed improvement preserves longitudinal symmetry; therefore, the 6DOF motion equations of the vehicle include the following components [13]:

1) Translational motion of the center of mass in the body frame:

$$\begin{bmatrix}\dot{u}\\ \dot{v}\\ \dot{w}\end{bmatrix}=\frac{1}{m}\begin{bmatrix}X\\ Y\\ Z\end{bmatrix}-\begin{bmatrix}0 & -r & q\\ r & 0 & -p\\ -q & p & 0\end{bmatrix}\begin{bmatrix}u\\ v\\ w\end{bmatrix} \tag{1}$$

where $[u, v, w]$, $[X, Y, Z]$ and $[p, q, r]$ denote velocity components, external forces, and angular rates in the body frame, respectively; m is the mass of the vehicle.

2) Rotational motion about the center of mass in the body frame:

$$\begin{bmatrix}\dot{p}\\ \dot{q}\\ \dot{r}\end{bmatrix}=\begin{bmatrix}1/I_{xx} & 0 & 0\\ 0 & 1/I_{yy} & 0\\ 0 & 0 & 1/I_{zz}\end{bmatrix}\left(\begin{bmatrix}L\\ M\\ N\end{bmatrix}-\begin{bmatrix}0 & -r & q\\ r & 0 & -p\\ -q & p & 0\end{bmatrix}\begin{bmatrix}I_{xx} & 0 & 0\\ 0 & I_{yy} & 0\\ 0 & 0 & I_{zz}\end{bmatrix}\begin{bmatrix}p\\ q\\ r\end{bmatrix}\right) \tag{2}$$

where *[L, M, N]* and *[I_{xx}, I_{yy}, I_{zz}]* are the external moments and moments of inertia.

3) Translational motion in the Earth-fixed frame

$$\begin{bmatrix}\dot{x} & \dot{y} & \dot{z}\end{bmatrix}^T=C_b^n\begin{bmatrix}u & v & w\end{bmatrix}^T \tag{3}$$

4) Rotational motion in the Earth-fixed frame:

$$\begin{bmatrix}\dot{\phi}\\ \dot{\theta}\\ \dot{\psi}\end{bmatrix}=\begin{bmatrix}1 & \sin\phi\tan\theta & \cos\phi\tan\theta\\ 0 & \cos\phi & -\sin\phi\\ 0 & \sin\phi/\cos\theta & \cos\phi/\cos\theta\end{bmatrix}\cdot\begin{bmatrix}p\\ q\\ r\end{bmatrix} \tag{4}$$

The external forces acting on the vehicle include gravitational force $\boldsymbol{F}_G$, aerodynamic forces on the body and lifting surfaces $\boldsymbol{F}_A$, and control aerodynamic forces on the control surfaces $\boldsymbol{F}_F$:

$$\begin{bmatrix}X\\ Y\\ Z\end{bmatrix}=\begin{bmatrix}X_G\\ Y_G\\ Z_G\end{bmatrix}+\begin{bmatrix}X_A\\ Y_A\\ Z_A\end{bmatrix}+\begin{bmatrix}X_F\\ Y_F\\ Z_F\end{bmatrix};\quad\begin{bmatrix}L\\ M\\ N\end{bmatrix}=\begin{bmatrix}L_A\\ M_A\\ N_A\end{bmatrix}+\begin{bmatrix}L_F\\ M_F\\ N_F\end{bmatrix} \tag{5}$$

Here, The external forces are defined by the following expresses:

$$\begin{bmatrix}X_G\\ Y_G\\ Z_G\end{bmatrix}=C_n^b\begin{bmatrix}0\\ 0\\ mg\end{bmatrix};\quad\begin{bmatrix}X_F\\ Y_F\\ Z_F\end{bmatrix}=\sum_{i=1}^{4}q_{din}S\begin{bmatrix}-CAd(M,\delta_i)\\ CYd(M,\delta_i)\sin\phi_i\\ -CNd(M,\delta_i)\cos\phi_i\end{bmatrix}\approx\sum_{i=1}^{4}q_{din}S\begin{bmatrix}-CAd(M,\delta_i)\\ CYD(M)\delta_i\sin\phi_i\\ -CND(M)\delta_i\cos\phi_i\end{bmatrix};$$

$$\begin{bmatrix} X_A \\ Y_A \\ Z_A \end{bmatrix} = \begin{bmatrix} -CA(M,\alpha_s,p,q,r) \\ CY(M,\beta,p,r) \\ CN(M,\alpha,\dot{\alpha},q) \end{bmatrix} q_{din}S \approx \begin{bmatrix} -CA(M,\alpha_s) \\ CYB(M)\beta + CYP(M)\bar{p} + CYR(M)\bar{r} \\ CNA(M)\alpha + CNAD(M)\dot{\bar{\alpha}} + CNQ(M)\bar{q} \end{bmatrix} q_{din}S;$$

$$\begin{bmatrix} L_A \\ M_A \\ N_A \end{bmatrix} = \begin{bmatrix} CLL(M,\beta,p,r) \\ CM(M,\alpha,\dot{\alpha},q) \\ CLN(M,\beta,p,r) \end{bmatrix} q_{din}SD \approx \begin{bmatrix} CLLB(M)\beta + CLLP(M)\bar{p} + CLLR(M)\bar{r} \\ CMA(M)\alpha + CMAD(M)\dot{\bar{\alpha}} + CMQ(M)\bar{q} \\ CLNB(M)\beta + CLNP(M)\bar{p} + CLN(M)\bar{r} \end{bmatrix} q_{din}SD;$$

$$\begin{bmatrix} L_F \\ M_F \\ N_F \end{bmatrix} = \sum_{i=1}^{4} q_{din}SD \begin{bmatrix} CLLd(M,\delta_i) \\ CMd(M,\delta_i)\cos\phi_i \\ CLNd(M,\delta_i)\sin\phi_i \end{bmatrix} \approx \sum_{i=1}^{4} q_{din}SD \begin{bmatrix} CLLD(M)\delta_i \\ CMD(M)\delta_i\cos\phi_i \\ CLND(M)\delta_i\sin\phi_i \end{bmatrix};$$

where *[ϕ, θ, ψ]* and *[p, q, r]* are Euler angles and its angular rates; α_s, α, β are the spatial angle of attack, angle of attack, and sideslip angle, respectively; q_{din}, S are the dynamic pressure and characteristic area, respectively; δ_i is the control surface deflection; D – GFV diameter.

The next task is to synthesize the guidance law and control law to achieve a predefined terminal impact angle.

2.3. Guidance and control law synthesis for the proposed scheme

2.3.1. Robust autopilot design

The GFV operates over an altitude range of 0–5 km, with velocity varying from 300 to 200 m/s. A correction filter is designed to ensure a gain margin of no less than 6 dB and a phase margin of no less than 35 degrees, providing robustness against disturbances and model parameter variations.

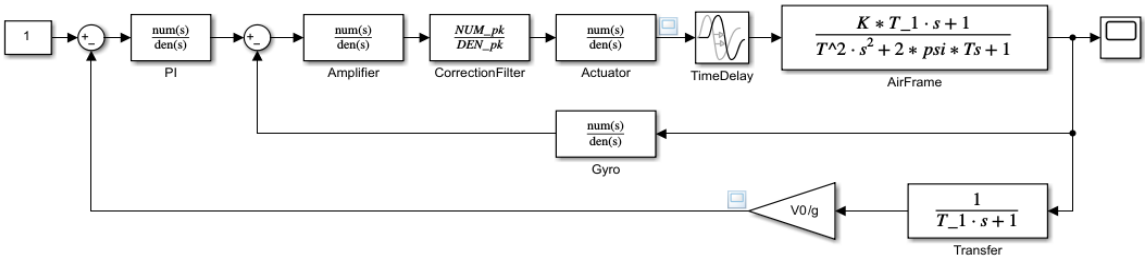

Figure 3. *Two-loop longitudinal autopilot for elevator displacement.*

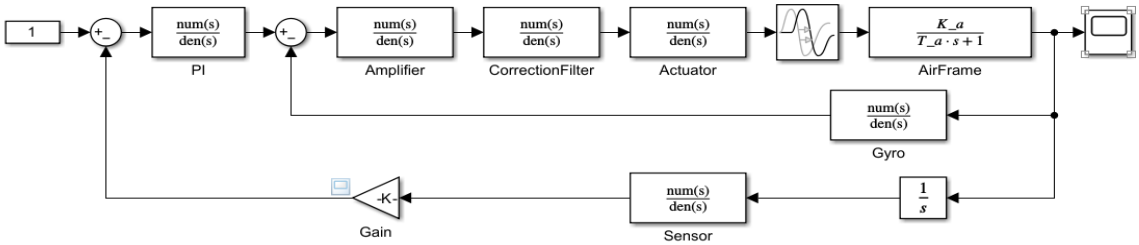

Figure 4. *Two-loop lateral autopilot for aileron displacement.*

Suppose, the GFV is equipped with angular rate gyros, accelerometers, and roll angle sensors. The two-loop autopilot structures for longitudinal and lateral motion are illustrated in Figures 3 and 4.

After linearizing the 6DOF equations, the vehicle transfer function is obtained as [14]:

$$W_{TL\_Long}(s)=\frac{\theta(s)}{\delta_e(s)}=\frac{K(T_1s+1)}{T^2s^2+2\xi Ts+1};\quad W_{TL\_Lat}(s)=\frac{\phi(s)}{\delta_a(s)}=\frac{K_a}{T_as+1} \tag{6}$$

Here, parameters in (6) depend on geometry, aerodynamic and inertial characterictics of GFV [14].

The actuator transfer function is modeled as [15]:

$$W_{ML}(s)=\frac{\delta(s)}{\delta_c(s)}=\frac{1}{T_{ml}^2s^2+2\xi_{ml}T_{ml}s+1}e^{-\tau s} \tag{7}$$

Here, parameters of actuator: $T_{ml}=0,25T;\quad \xi_{ml}$=0,7; $\quad \tau=5ms.$

The angular rate gyro is represented by a second-order transfer function [15]:

$$W_{CQ}(s)=\frac{p_s(s)}{p(s)}=\frac{1}{T_{cq}^2s^2+2\xi_{cq}T_{cq}s+1} \tag{8}$$

Here, parameters of angular rate gyro: $T_{cq}=10ms;\quad \xi_{cq}$=0,7.

The amplifier transfer function is given by [15]:

$$W_{KD}(s)=\frac{U(s)}{\Delta p(s)}=\frac{K_{kd}}{T_{kd}s+1} \tag{9}$$

Here, parameters of Amplifier: $K_{kd}=100/K;\quad T_{kd}=1ms.$

Desired open-loop frequency characteristics are defined as shown in Figures 5 and 6, with the open-loop transfer function expressed as [16]:

$$W_{m\_Long}=\frac{100(T_1s+1)(T_Cs+1)}{(T_Bs+1)^3(T_Ds+1)^4(T_{kd}s+1)};\quad W_{m\_Lat}=\frac{100(T_Cs+1)}{(T_Bs+1)^2(T_Ds+1)^4(T_{kd}s+1)} \tag{10}$$

The correction filter transfer function is then derived as:

$$W_{pk}(s)=\frac{W_m(s)}{W_{KD}(s)W_{ML}(s)W_{TL}(s)W_{CQ(s)}} \tag{11}$$

Bode plots of the inner loop after applying the correction filter shown in Figs. 7 and 8.

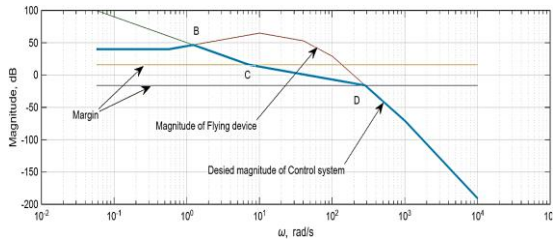

Figure 5. *Definition of desied magnitude characteristic of longitudinal autopilot.*

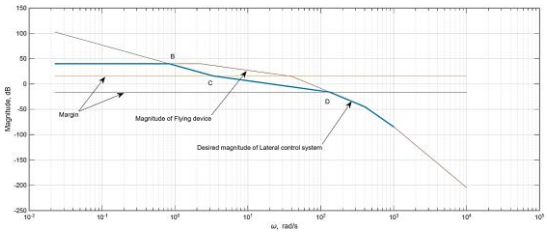

Figure 6. *Definition of desied magnitude characteristic of lateral autopilot.*

The correction filter transfer function is then derived as:

$$W_{pk}(s)=\frac{W_m(s)}{W_{KD}(s)W_{ML}(s)W_{TL}(s)W_{CQ(s)}} \tag{12}$$

Bode plots of the inner loop after applying the correction filter shown in Figs. 7 and 8.

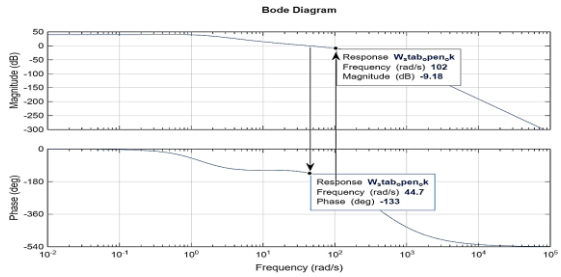

Figure 7. *Inner loop Bode diagram of longitudinal autopilot.*

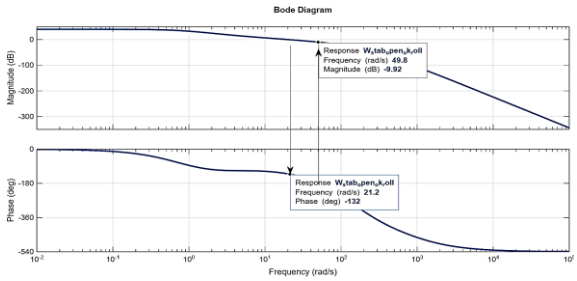

Figure 8. *Inner loop Bode diagram of lateral autopilot.*

To reduce steady-state error, a PI compensator is added in the outer loop. Time-domain step responses of the autopilot are illustrated in Figures 9 and 10.

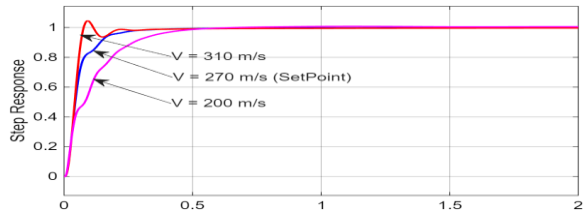

Figure 9. *Step response of longitudinal autopilot.*

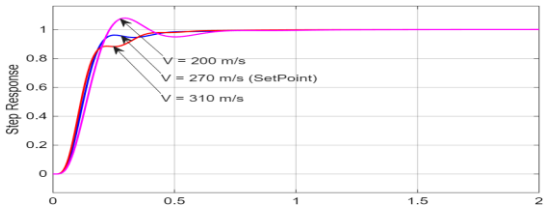

Figure 10. *Step response of lateral autopilot.*

Key observations: From Figures 9 and 10, it is easy to see that the step response at the set point is the best. At the upper (310 m/s) and lower (200 m/s), the step response decreases compared to the set point (overshoot and settling time), however, the correction filter still ensures the convergence of the autopilot.

2.3.2. Guidance law synthesis

For the extended-range configuration, to ensure a specified terminal impact angle in the vertical plane, a shaping guidance law (SGL) [16] is employed instead of the conventional proportional navigation (PN):

$$n_y(t) = 4V_{TL}(t)\dot{\sigma}_y(t); \quad n_z(t) = 4V_{TL}(t)\dot{\sigma}_z(t) + \frac{2V_{TL}^2(t)}{R(t)}\left[\sigma_z(t) - \sigma_{Des}\right] \tag{13}$$

where, $\sigma(t)$ is the line-of-sight (LOS) angle; V_{TL} is the vehicle velocity, and $R(t)$ is the current distance to the target.

The guidance law (13) was chosen because the following reason: To attack a fixed target with the desired impact angle, as [16] the author has proven on the basis of Schwartz inequality, the shaping guidance law is the most energy-efficient solution.

Since the TV seeker cannot directly measure $R(t)$, it is approximated as:

$$R(t) = R_0 - V(t) * t \tag{14}$$

This approximation directly affects the second component in formula (13), which is the accuracy of the impact angle. However, in practice, a small deviation of the impact angle from the desired value is allowed, so the improvement solution according to formula (14) is entirely feasible.

Based on these formulations, a MATLAB-based simulation is developed to validate the proposed improvement scheme.

3. RESULTS AND DISCUSSION

3.1. Simulation input data

Simulation parameters include:

1) Geometric, mass, and inertia parameters:: D = 0,350m; L = 3,045m; CG = 1,55m; Ixx = 7,96 kg.m^2; Iyy = 407,09 kg.m^2;

2) Aerodynamic coefficients: obtained using Missile DATCOM. Survey range for March number: 0.1 to 0.95. Survey range for angle of attack: -10^0 to 10^0;

3) Initial flight conditions: V_0 = 1100 km/h; r_0 = [0, 0, -5000] m; Euler$_0$ = [0, 5, 0] deg.

The MATLAB/Simulink simulation architecture is shown in Figure 11. Two scenarios are considered: a 9 km range for comparison original case and a 16 km extended-range case. Both PN and SGL guidance laws are evaluated with a terminal impact angle of 45 degrees. The GFVs stabilized after separating from the aircraft and self-guided to the target after 2.6 seconds.

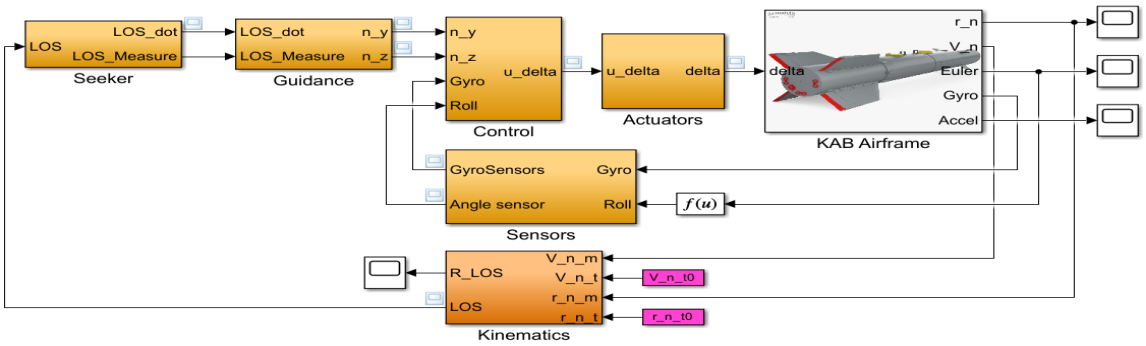

Figure 11. *6DOF motion simulation program.*

3.2. Simulation results and comments

3.2.1. Results at 9 km range

Simulation results for the improved GFV using PN and SGL at a 9 km range are shown in Figures 12–17.

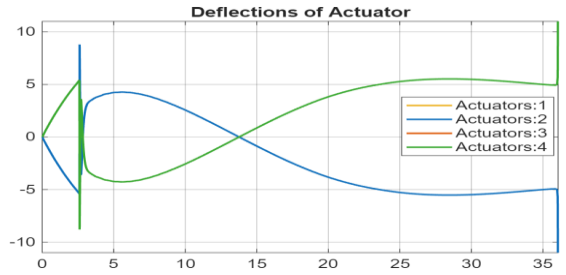

Figure 12. *Graph of fin angles of PN.*

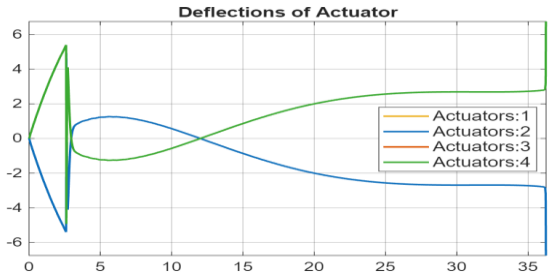

Figure 13. *Graph of fin angles of SGL.*

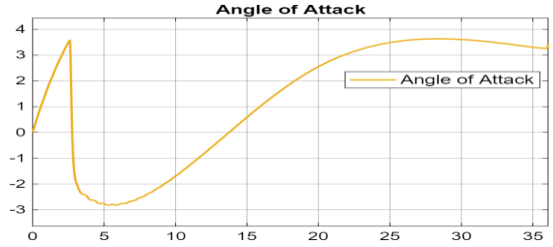

Figure 14. *Graph of angle of attack with PN.*

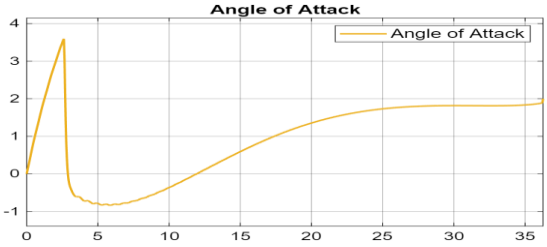

Figure 15. *Graph of angle of attack with SGL.*

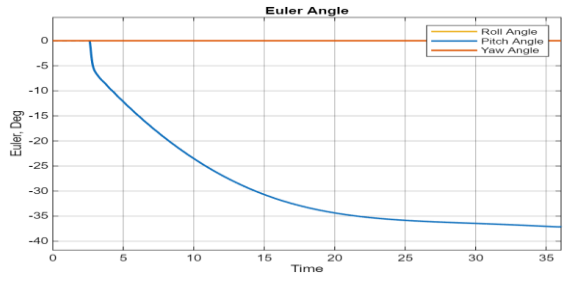

Figure 16. *Graph of Euler angles of PN.*

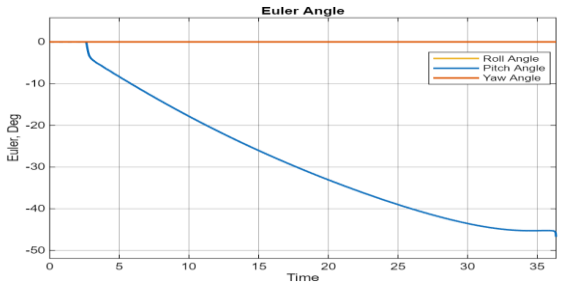

Figure 17. *Graph of Euler angles of SGL.*

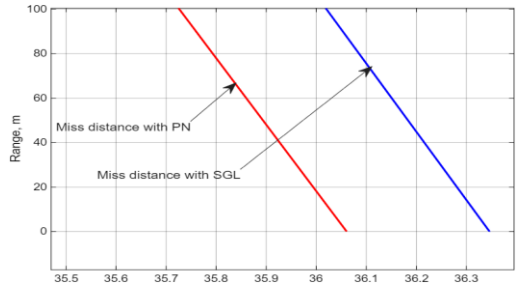

Figure 18. *Miss distance of PN and SGL.*

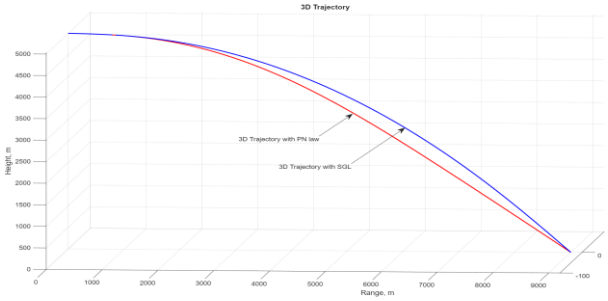

Figure 19. *3D trajectories of PN and SGL.*

Key observations:

- The miss distance at impact point is approximately zero in both cases, validating the correctness of the synthesized guidance and control system.

- With SGL, the pitch angle at impact closely matches the prescribed value of 45 degrees, whereas PN yields approximately 37 degrees.

- Due to its trajectory being closer to a ballistic path, SGL requires smaller control surface deflections than PN. However, increasing the area of the leading wing simultaneously increases lift force and reduces static stability margin, meaning the control effect is enhanced compared to the original design at the same control surface deflections.

3.2.2. Results at 16 km range

Results for the 16 km extended-range case are shown in Figures 18–23.

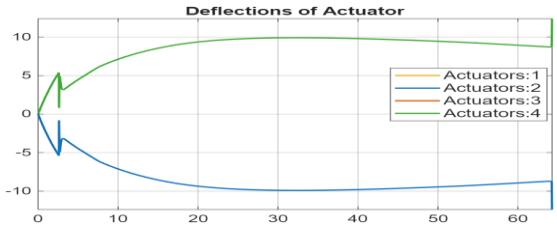

Figure 20. *Graph of fin angles of PN.*

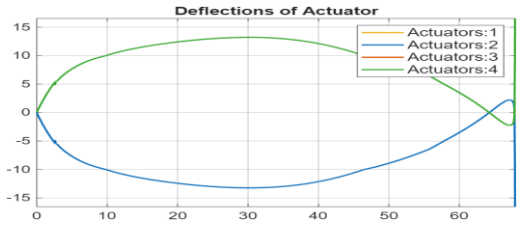

Figure 21. *Graph of fin angles of SGL.*

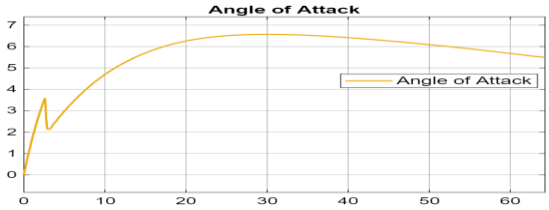

Figure 22. *Graph of angle of attack with PN.*

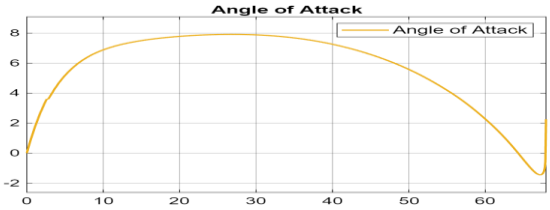

Figure 23. *Graph of angle of attack with SGL.*

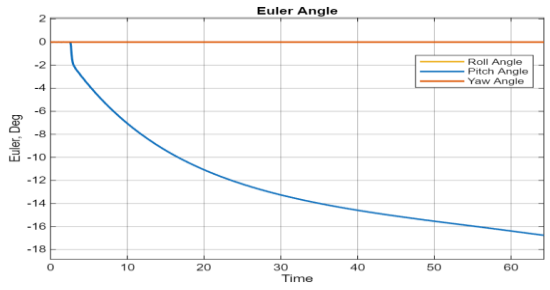

Figure 24. *Graph of Euler angles of PN.*

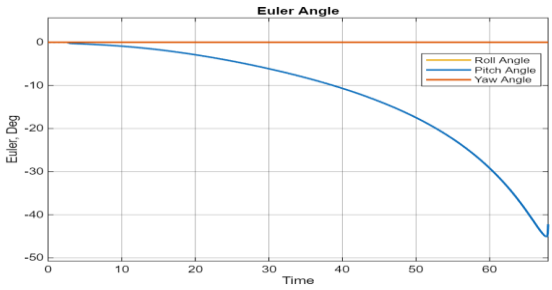

Figure 25. *Graph of Euler angles of SGL.*

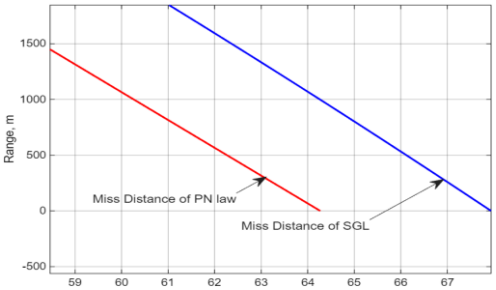

Figure 26. *Miss distance of PN and SGL.*

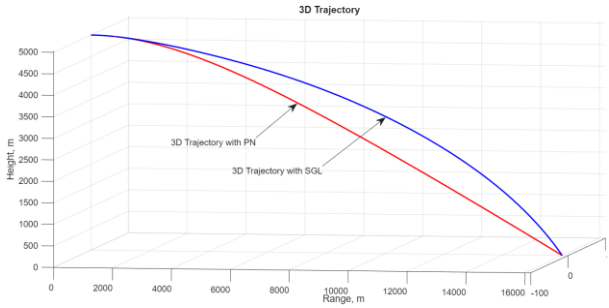

Figure 27. *3D trajectories of PN and SGL.*

Key observations:

- The miss distance remains near zero, confirming the validity of the proposed extended-range solution. The impact pitch angle with SGL remains close to 45 degrees, whereas PN results in approximately 17 degrees, which is insufficient for top-attack profiles.

- SGL requires larger control surface deflections due to trajectory shaping demands during the extended-range phase.

- Original design has limited control effects, preventing it from achieving a range of 16 km. The proposed design solution enhances control effects to maintain gliding flight trajectory; therefore, simulation results have shown that the improved GFV increases its effective range to 16 km while maintaining accuracy and a desired impact angle.

Acknowledgment: The authors sincerely thank the Ministry of Defence project, code number 2024.85.32, for its support in conducting this study.

4. CONCLUSIONS

Based on aerodynamic analysis, this paper proposes an extended-range improvement solution for a TV-homing HFV released from an aircraft. To validate the proposed approach, a complete guidance and control system was synthesized and verified using a 6DOF motion model of the modified GFV.

To ensure controller robustness under dynamic parameter variations, a correction filter based on desired frequency-domain characteristics was designed. Furthermore, the conventional PN guidance law was replaced by a SGL to guarantee the required terminal impact angle.

Simulation results confirm the effectiveness of the proposed solution, enabling the GFV to extend its operational range from 9 km to 16 km while maintaining a terminal impact angle of no less than 45 degrees. The guidance and control laws were synthesized based on a linearized vehicle model to validate the improvement solution. Future work will investigate the application of modern control theory to further enhance controller performance.

Acknowledgment: The authors sincerely thank the Ministry of Defence project, code number 2024.85.32, for its support in conducting this study.

REFERENCES

[1]. Aly S. Attallah et al., *"Attitude Control of Gliding Bomb using Classical PID and Modified PI-D Controllers"*, Journal of Multidisciplinary Engineering Science and Technology (JMEST), Vol. 3, No. 4, (2016).

[2]. Islam H. Elandy et al., *"Modeling and Simulation of an Aerial Gliding Body in Free-Fall"*, International Journal of Engineering Research & Technology (IJERT), Vol. 7, No. 8, (2018).

[3]. Muhammed et al., *"Design and Simulation of the Guidance and Control System for Gliding Munitions"*, Dicle University Journal of Engineering, Vol. 15, No. 2, pp. 285-291, (2024).

[4]. Е. А. Федосов, *"Высокоточная бомба малого калибра SDB (США)"*, Научно-информационный центр ГосНИИАС, Москва, (2016).

[5]. Asaf Sayıl et al., *"The History of Guided Bombs, Guidance Kits, Wing Kits, and Wing Deployment Mechanisms"*, Journal of Aeronautics and Space Technologies, Vol. 17, No. 2, pp. 203-234, (2024).

[6]. Marta Grzyb et al., *"Analysis of a Hybrid Guided Bomb Control System while Self-guided to a Ground Target"*, Problems of Mechatronics Armament Aviation Safety Engineering, (2019).

[7]. Grzegorz Kowaleczko et al., *"Evaluation of the Possibility of Bomb Flight Control"*, Journal of KONES Powertrain and Transport, Vol. 22, No. 3, (2015).

[8]. Ahmed S. Gad, *"Smart bomb's guidance loop design"*, Proc. 8th ASAT Conference, Cairo, pp. GC-02, (1999).

[9]. Ahmad Mahmood et al., *"Trajectory Optimization of a Subsonic Unpowered Gliding Vehicle Using Control Vector Parameterization"*, Drones, Vol. 6, art. no. 360, (2022).

[10]. Ahmad Mahmood et al., *"Optimal Standoff Distance of Subsonic Unpowered Gliding Vehicle"*, Results in Control and Optimization, Vol. 12, (2023).

[11]. Gian Marco Vinco, *"Flight Dynamics Modeling and Autopilot Design for Guided Projectiles via Linear Parameter-Varying Techniques"*, HAL open science, (2024).

[12]. Nguyen Van Khoi et al., *"Simulation of 6DOF motion control loop of three-channel flight device"*, Journal of Military Science and Technology, Vol. 101, pp. 3-12, (2025).

[13]. John H. Blakelock, *Automatic Control of Aircraft and Missiles*. A Wiley-Interscience Publication, Second Edition, (1991).

[14]. Qi Zaikang, *Design of Guidance and Control Systems for Tactical Missiles*. CRC Press Taylor & Francis Group, (2020).

[15]. Paul Zarchan, *Tactical and Strategic Missile Guidance*. Progress in Astronautics and Aeronautics, Vol. 239, (2012).

[16]. В. В. Солодовников, В. Н. Плотников, А. В. Яковлев, *Теория автоматического управления техническими системами*. Изд-во МГТУ, 492 с., (1993).

TÓM TẮT

Giải pháp cải tiến tăng tầm cho thiết bị bay tự dẫn

Bài báo trình bày một giải pháp cải tiến tăng tầm cho thiết bị bay (TBB) có điều khiển sử dụng đầu tự dẫn TV bằng cách tăng diện tích cánh nâng trong phạm vi cho phép bảo đảm tính ổn định của TBB. Việc thay đổi này đồng nghĩa với yêu cầu thiết kế lại bộ điều khiển theo cấu hình khí động học mới. Ngoài ra, vận tốc và độ cao TBB thay đổi lớn trong quá trình bay lượn tăng tầm nên bộ điều khiển được thiết kế cần bảo đảm tính bền vững trong toàn bộ dải vận tốc cũng như ảnh hưởng của nhiễu động bên ngoài. Kết quả mô phỏng chuyển động 6DOF cho thấy, giải pháp cải tiến và bộ điều khiển xây dựng cho phép TBB tăng tầm bay từ 9 km đến 16 km với góc va chạm không nhỏ hơn 45 độ.

Từ khoá: TBB lượn tăng tầm; Tổng hợp bộ điều khiển; 6DOF simulation.